Journal of Electrotechnology, Electrical Engineering and Management (2026)
Clausius Scientific Press, Canada
DOI: 10.23977/jeeem.2026.090102
ISSN 2560-6697 Vol. 9 Num. 1

A Refined Approach to Position Estimation in Sensorless Control of IPMSM Drives with Small DC-Link Capacitor Drive System

Wenjing Fan[a]

Dept. of Electrical and Control Engineering, Xi'an University of Science and Technology, Xi'an 710600, Shaanxi Province, China
[a]*fanwenjing@xust.edu.cn*

Keywords: Permanent magnet synchronous motor; small DC-link capacitor drive system; model-reference-adaptive; super-twisting sliding-mode sensorless

Abstract: To address harmonic-induced speed fluctuations in small DC-link capacitor drive systems, an improved Super-Twisting-Algorithm Adaptive Observer (STA-AO) is proposed for sensorless IPMSM control. It replaces the conventional PI mechanism in a model-reference-adaptive system (MRAS) observer with a super-twisting sliding-mode algorithm. This enhances robustness, accelerates error convergence, and improves dynamic response under system parameter variations. Simulations and experiments on a drive with small film capacitors demonstrate that the STA-AO significantly increases rotor position and speed estimation accuracy. It reduces feedback loop errors, improves modulation waveforms, and suppresses current harmonics, thereby enhancing overall control stability and performance.

1. Introduction

Interior Permanent Magnet Synchronous Machines (IPMSM) are widely used in aerospace, industry, and household appliances for their high efficiency, compactness, and light weight [1-4]. Traditional IPMSM drives rely on large electrolytic capacitors (hundreds to thousands of μF) to stabilize DC-link voltage, but these occupy 20%-40% of high-power drive volume and risk electrolyte evaporation, reducing system reliability [5-6]. Film capacitors, by contrast, offer longer lifespans and smaller sizes, spurring research on electrolytic-capacitor-less (ECL) drives—where small film capacitors replace electrolytic ones [7-11]. However, small capacitors fail to maintain constant DC-link voltage, causing double-grid-frequency fluctuations that challenge IPMSM control [12].

Traditional ECL drives use power factor correction (PFC) circuits to reduce grid harmonics, but this increases cost and volume [13-15]. Removing PFC requires the inverter to regulate grid current harmonics and power factor. Sensorless control (effective in traditional drives [16-17]) can further miniaturize ECL systems and boost reliability, but DC-link voltage fluctuations in ECL drives introduce harmonics that degrade control performance and sensorless observation accuracy [18-19].

The key challenge for sensorless ECL drives is mitigating signal fluctuation effects. Existing methods (e.g., sliding-mode observers [20-21], synchronous filters [22], fast sliding-mode observers [23]) do not address ECL-specific voltage/current fluctuations or suffer from coordinate

errors/insufficient robustness.

MRAS-based sensorless control is valued for simplicity and anti-interference, but faces accuracy issues from parameter fluctuations and sliding-mode chattering [24-26]. This study proposes an MRAS-based sensorless approach tailored to ECL drives: the STA-AO (Super-Twisting-Algorithm Adaptive Observer). Replacing the traditional MRAS PI adaptive mechanism with the Super-Twisting-Algorithm (STA) mitigates sliding-mode chattering, improving position observation accuracy, speed estimation dynamic performance, and robustness against ECL system fluctuations.

2. IPMSM drive system small DC-link capacitors

2.1. Characteristic analysis of electrolytic capacitor-less drive system

The diagram in Fig. 1 illustrates the IPMSM drive system powered by a single-phase diode rectifier and a small DC link capacitor. This system comprises an uncontrolled rectifier bridge, DC-link film capacitor, inverter, and motor.

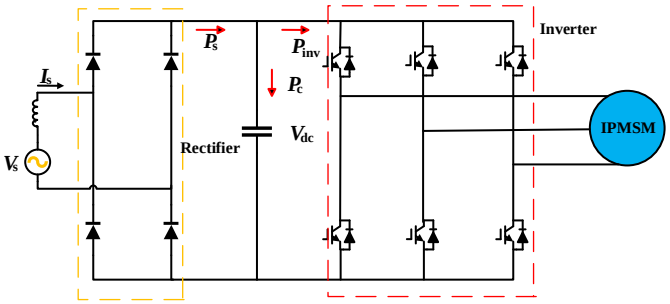

Fig. 1. Topology of small DC-link capacitor IPMSM drive system

Due to the decreased DC-link capacitance, the DC-link voltage fluctuates at twice the frequency of the grid voltage. Assuming the grid voltage follows an ideal sinusoidal waveform, the ideal grid input current (I_s) and the grid-side input voltage (V_s) can be expressed as follows:

$$I_s = I_{sm}\sin\left(\omega_s t+\theta_s\right) \tag{1}$$

$$V_s = V_{sm}\sin\left(\omega_s t+\theta_s\right) \tag{2}$$

The formula is as follows: I_{sm} and V_{sm} represent the maximum values of the input current and voltage from the grid, while ω_s and θ_s denote the grid-frequency and initial phase, respectively. The input power on the grid side can be expressed as:

$$P_s = V_{sm}I_{sm}\sin^2(\omega_s t+\theta_s) = P_{inv}+P_c \tag{3}$$

In the formula: P_{inv} represents the power of the inverter, and Pc represents the power of the capacitor.

Disregarding the voltage drop of the grid side rectifier diode, the DC-link capacitor voltage equals the absolute value of the grid voltage. The DC-link voltage can be expressed as:

$$V_{dc} = V_{sm}\sin(\omega_s t+\theta_s)\mathrm{sgn}(\omega_s t+\theta_s) \tag{4}$$

In the formula: sgn(x) represents the sign function.The capacitance current i_c can be calculated as follows.

$$i_c = C_{dc}\frac{dV_{dc}}{dt} = \omega_s C_{dc}V_{sm}\cos(\omega_s t+\theta_s)\mathrm{sgn}(\omega_s t+\theta_s) \tag{5}$$

In the formula ： C_{dc} represents the capacity of the DC-link film capacitor. The expression of the DC-link capacitor power Pc can be calculated as follows:

$$P_c = \frac{1}{2}\omega_s C_{dc} V_{sm}{}^2 \sin(2(\omega_s t + \theta_s)) \tag{6}$$

The expression for the inverter output power can be calculated as follows:

$$\begin{aligned} P_{inv} &= V_{sm}\sin(\omega_s t+\theta_s)\mathrm{sgn}(\omega_s t+\theta_s) - \omega_s C_{dc} V_{sm}\cos(\omega_s t+\theta_s)\mathrm{sgn}(\omega_s t+\theta_s) \\ &= \frac{1}{2}V_{sm}I_{sm} - \frac{1}{2}V_{sm}\sqrt{(I_{sm}{}^2 + \omega_s{}^2 C_{dc}{}^2)}\sin(2(\omega_s t+\theta_s) + \arctan\frac{I_{sm}}{\omega_s C_{dc} V_{sm}} \end{aligned} \tag{7}$$

Upon inspection of Equation (7), it becomes evident that the output power of the inverter in the electrolytic capacitor-less drive system varies periodically at twice the grid-frequency. Based on this power expression, the power relationship waveform within a grid voltage cycle is illustrated. Fig. 2 delineates the correlation among the grid-side input power, the DC-link voltage, and the inverter input power.

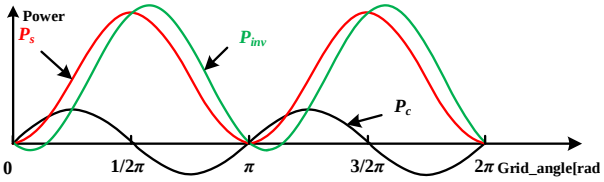

Fig. 2. Power relationship diagram

Given that the motor inductance only engages in energy exchange over a DC-link voltage cycle, with an average power of zero, the inverter's output power can be approximated as equal to the motor's electromagnetic power. The expression for the inverter output power is as follows:

$$P_{inv} \approx P_{em} = T_{em}\omega_r \tag{8}$$

Due to the presence of rotational inertia, the mechanical angular velocity ω_r is maintained at a constant value during stable motor operation. Additionally, the electromagnetic torque is directly proportional to the q-axis current. According to (8), the q-axis current waveform of the motor bears resemblance to the inverter's output power waveform. Based on the inverter's output power waveform depicted in Fig. 2, the q-axis current is approximated as:

$$i_q = i_{q\_av} - i_{q\_av}\cos 2\theta_s \tag{9}$$

In the formula: i_{q-av} represents the average value of q-axis current and the amplitude of AC component. The The root mean square (rms)q-axis current iq_rms can be calculated as follows:

$$i_{q\_rms} = \sqrt{\frac{1}{\pi}\int_0^{\pi}(i_{q\_av} - i_{q\_av}\cos 2\theta_s)^2 d\theta_s} = \sqrt{\frac{3}{2}}i_{q\_av} \tag{10}$$

From Equation (10), it is evident that in the small DC-link capacitor drive system, the root mean square value of the q-axis current is $\sqrt{\frac{3}{2}}$ times its average value, whereas in the traditional drive system, the q-axis current of the motor is constant and its average value equals the effective value.

Since the motor torque is linear with the q-axis current, the motor torque will also fluctuate at twice the grid-frequency, which can be approximately expressed as:

$$T_{em} = T_{av} - T_{av}\cos 2\theta_s \tag{11}$$

In the formula: T_{av} represents the average torque of the motor.By substituting Equation (11) into

the motor's mechanical motion equation, we can derive:

$$\frac{d\omega_r}{dt} = -\frac{T_{av}\cos 2\theta_s}{J} \tag{12}$$

By solving the preceding equation and incorporating it into the correlation between the motor speed (n) and the mechanical angular velocity (ω_r), we can express the connection between the speed (n) fluctuation range and the average torque and rotational inertia of the motor as:

$$\Delta n = \frac{3T_{av}}{20\pi^2 J} \tag{13}$$

Based on the above analysis, it is evident that the DC-link voltage fluctuation in the small DC-link capacitor drive system will influence various aspects of the motor, including speed, torque, and other factors.

2.2. Influence of DC-link voltage fluctuation on sensorless control technology

Following the preceding analysis, the DC DC-link voltage can be expressed as:

$$V_{dc} = V_{\mathrm{dc0}} + V_{dc1}\sin(2\omega_s t + \theta_{dc1}) \tag{14}$$

As the DC link voltage undergoes periodic fluctuation, it influences the three-phase stator voltage. When higher harmonics are disregarded and SVPWM control is employed, the three-phase voltage can be expressed as:

$$\begin{bmatrix} u_{an} \\ u_{bn} \\ u_{cn} \end{bmatrix} = \frac{V_{dc}}{3}\begin{bmatrix} 2 & -1 & 1 \\ -1 & 2 & -1 \\ -1 & -1 & 2 \end{bmatrix}\begin{bmatrix} S_a \\ S_b \\ S_c \end{bmatrix} \tag{15}$$

In the formula: When (S_x= 1), it indicates that the corresponding inverter is in a break-over state. Conversely, when (S_x= 0), it signifies the turn-off condition.

By transforming from the natural coordinate system to the rotating coordinate system, the dq-axis voltage can be calculated as follows:

$$\begin{aligned} \begin{bmatrix} u_d \\ u_q \end{bmatrix} &= C_{3s-2r}\begin{bmatrix} u_{an} \\ u_{bn} \\ u_{cn} \end{bmatrix} \\ &= \frac{2}{3}\begin{bmatrix} \sin\theta & \sin(\theta-\frac{2}{3}\pi) & \sin(\theta+\frac{2}{3}\pi) \\ \cos\theta & \cos(\theta-\frac{2}{3}\pi) & \cos(\theta-\frac{2}{3}\pi) \end{bmatrix}\frac{V_{dc}}{3}\begin{bmatrix} 2 & -1 & 1 \\ -1 & 2 & -1 \\ -1 & -1 & 2 \end{bmatrix}\begin{bmatrix} S_a \\ S_b \\ S_c \end{bmatrix} \\ &= \begin{bmatrix} -\frac{2}{3}\cos\theta + \frac{1}{\sqrt{3}}\sin\theta & \frac{1}{3}\cos\theta + \frac{2}{\sqrt{3}}\sin\theta & \frac{1}{3}\cos\theta \\ \frac{2}{3}\sin\theta + \frac{1}{\sqrt{3}}\cos\theta & -\frac{1}{3}\sin\theta + \frac{2}{\sqrt{3}}\cos\theta & -\frac{1}{3}\sin\theta \end{bmatrix}\begin{bmatrix} S_a \\ S_b \\ S_c \end{bmatrix}V_{\mathrm{dc}} \end{aligned} \tag{16}$$

The equation above indicates that the DC-link voltage leads to the influence of double-frequency harmonics of u_d and u_q. These values, obtained through Park inverse transformation to u_α and u_β, also contain harmonics. The input quantity of the position-sensorless technology includes u_α and u_β. Therefore, bus voltage fluctuation will reduce the observation accuracy of the position-sensorless control technology. This will lead to estimation errors when calculating the speed. When the speed estimation is integrated and accumulated, position estimation errors are inevitable.

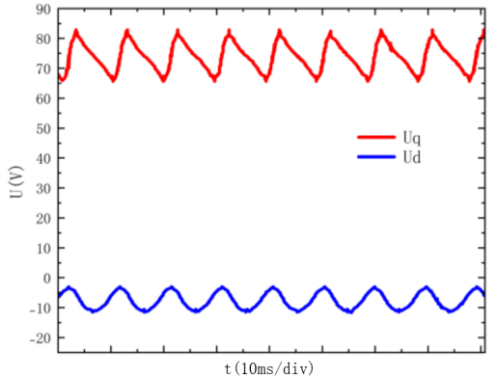

Fig. 3. Simulation diagram of each voltage component in d-q coordinate system

Likewise, there are current fluctuations at twice the grid-frequency. According to the nodal current law, the relationship between the currents in the simplified circuit model is as follows:

$$i_s = i_c + i_{inv} \tag{17}$$

In the actual drive system, the motor voltage is generated using pulse width modulation (PWM) technology, and the inverter power transistor switching state is consistently altered at a high-frequency. Consequently, the instantaneous current i_{inv} of the input inverter can be expressed as follows:

$$i_{inv} = s_a i_a + s_b i_b + s_c i_c \tag{18}$$

In the formula: i_a、i_b、i_c represent the three-phase current of the motor respectively.

The conduction state of the three-phase bridge arm of the inverter is indicated by the high-frequency switching signal, resulting in the actual input current of the inverter containing high-frequency harmonics related to the switching frequency. In traditional motor drive systems, large electrolytic capacitors in the bus act as filters for high-frequency current harmonics generated by the inverter. However, the DC bus film capacitors in electrolytic capacitor-free drive systems have limited filtering capabilities, causing a large number of current harmonics to flow into the power grid. These high-order harmonics are superimposed on the voltage and current signals of the motor, resulting in high-frequency noise in these signals. Sensorless control methods rely on accurate current and voltage signals for calculation, which affects the accuracy of the position sensor.

3. Sensorless model of electrolytic capacitor-less drive system

3.1. Sensorless model without electrolytic capacitor based on traditional MRAS observer

The state current equation of IPMSM in d-q axis is as follow:

$$\begin{cases} \dfrac{d}{dt} i_d = -\dfrac{R_s}{L_d} i_d + \omega_e \dfrac{L_q}{L_d} i_q + \dfrac{1}{L_d} u_d \\ \dfrac{d}{dt} i_q = -\dfrac{R_s}{L_q} i_q - \omega_e \dfrac{L_d}{L_q} i_d - \omega_e \dfrac{\psi_f}{L_q} + \dfrac{1}{L_q} u_q \end{cases} \tag{19}$$

In the above formula: u_d and u_q represent the stator voltage components of the d-q axes; R_s signifies the stator resistance; L_d and L_q denote the stator inductance components of the d-q axes; i_d and i_q denote the d-q axis stator current components; ω_e represents the electrical angular velocity of the rotor; and ψ_f signifies the permanent magnet flux linkage.

To derive the adjustable model, the state current equation can be transformed into:

$$\begin{cases} \dfrac{d}{dt}(i_d + \dfrac{\psi_f}{L_d}) = -\dfrac{R_s}{L_d}(i_d + \dfrac{\psi_f}{L_d}) - \omega_e \dfrac{L_d}{L_q} i_q + \dfrac{1}{L_d}(u_d + \dfrac{R_s \psi_f}{L_q}) \\ \dfrac{d}{dt} i_q = -\omega_e \dfrac{L_d}{L_q}(i_d + \dfrac{\psi_f}{L_d}) - \dfrac{R_s}{L_q} i_q + \dfrac{1}{L_q} u_q \end{cases} \tag{20}$$

In this equation: $i_d^{'} = i_d + \dfrac{\psi_f}{L_d}$, $i_q^{'} = i_q$, $u_d^{'} = u_d + \dfrac{R_s \psi_f}{L_q}$, $u_q^{'} = u_q$, Substituted into the above formula and written in matrix form:

$$\frac{d}{dt}\begin{bmatrix} i_d^{'} \\ i_q^{'} \end{bmatrix} = \begin{bmatrix} -\dfrac{R_s}{L_d} & \omega_e \dfrac{L_d}{L_q} \\ -\omega_e \dfrac{L_d}{L_q} & -\dfrac{R_s}{L_q} \end{bmatrix} \begin{bmatrix} i_d^{'} \\ i_q^{'} \end{bmatrix} + \begin{bmatrix} \dfrac{1}{L_d} & 0 \\ 0 & \dfrac{1}{L_q} \end{bmatrix} \begin{bmatrix} u_d^{'} \\ u_q^{'} \end{bmatrix} \tag{21}$$

Equation (21) reveals that the current state equation incorporates the rotor speed position information and motor-related parameters, utilizing the PMSM itself as the reference model, where is the estimated rotor electric angular velocity. By neglecting the effect of the deviation between the estimated and actual values, the adjustable model is expressed in matrix form:

$$\frac{d}{dt}\begin{bmatrix} \hat{i}_d^{'} \\ \hat{i}_q^{'} \end{bmatrix} = \begin{bmatrix} -\dfrac{R_s}{L_d} & \hat{\omega}_e \dfrac{L_d}{L_q} \\ -\hat{\omega}_e \dfrac{L_d}{L_q} & -\dfrac{R_s}{L_q} \end{bmatrix} \begin{bmatrix} \hat{i}_d^{'} \\ \hat{i}_q^{'} \end{bmatrix} + \begin{bmatrix} \dfrac{1}{L_d} & 0 \\ 0 & \dfrac{1}{L_q} \end{bmatrix} \begin{bmatrix} \hat{u}_d^{'} \\ \hat{u}_d^{'} \end{bmatrix} \tag{22}$$

The generalized state error is defined as follows:

$$error_d = i^{'} - \hat{i}^{'} \tag{23}$$

In the formula: $i^{'} = \begin{bmatrix} i_d^{'} \\ i_q^{'} \end{bmatrix}; \hat{i}^{'} = \begin{bmatrix} \hat{i}_d^{'} \\ \hat{i}_q^{'} \end{bmatrix}$.Subtracting Equation (21) from Equation (22) yields:

$$\frac{d}{dt} error_d = A_e e - B \tag{24}$$

In the formula:

$$A_e = \begin{bmatrix} -\dfrac{R_s}{L_d} & \hat{\omega}_e \dfrac{L_d}{L_q} \\ -\hat{\omega}_e \dfrac{L_d}{L_q} & -\dfrac{R_s}{L_q} \end{bmatrix}; B = \begin{bmatrix} 0 & \dfrac{L_q}{L_d} \\ -\dfrac{L_d}{L_q} & 0 \end{bmatrix} (\hat{\omega}_e . - \omega_e); \begin{bmatrix} \hat{i}_d^{'} \\ \hat{i}_q^{'} \end{bmatrix} = C_e(\hat{\omega}_e - \omega_e)\hat{i}^{'}; C_e = \begin{bmatrix} 0 & \dfrac{L_q}{L_d} \\ -\dfrac{L_d}{L_q} & 0 \end{bmatrix}$$

For the MRAS setup, the adaptive law typically incorporates a PI regulator to fine-tune the output of the adjustable model for system stability. The control block diagram is illustrated in Fig. 3. The adaptive law for motor angular velocity identification is assumed to be:

$$\hat{\omega}_e = \int_0^t F_1(v,t,\tau) + F_2(v,t) + \hat{\omega}_e(0) \tag{25}$$

The term $\hat{\omega}_e(0)$ represents the initial value of the estimated electrical angular velocity.

According to the Popov hyperstability theory, for the feedback system to be stable, the forward

channel transfer matrix must be positive definite, as reflected in the following expression:

$$F_1(v,t,\tau)=k_i f^{'}(t)=k_i e^T C_e \hat{i}^{'} \text{、} F_2(v,t)=k_p e^T C_e \hat{i}^{'} \tag{26}$$

The formulated adaptive law adheres to the Popov hyperstability theory, ensuring the nonlinear feedback system tends toward asymptotic stability and proficiently estimates the electrical angular velocity of the motor. The speed estimation equation is typically acquired using a PI adaptive law：

$$\begin{aligned}&\hat{\omega}_e=\hat{\omega}_e(0)+[k_p+\frac{k_i}{s}]\\&[\frac{L_q}{L_d}i_d\hat{i}_q-\frac{L_d}{L_q}i_q\hat{i}_d-\frac{\psi_f}{L_q}(i_q-\hat{i}_q)+i_d\hat{i}_q(\frac{L_d}{L_q}-\frac{L_q}{L_d})\end{aligned} \tag{27}$$

The rotor position can be represented as:

$$\hat{\theta}_e=\int\hat{\omega}_e\,dt \tag{28}$$

Based on the traditional MRAS observer, the rotor position estimation system block diagram is shown in Fig 4. The adaptive law receives the actual d-q axis currents $i_d$and $i_q$from the reference model output, as well as the estimated d-q axis currents$\hat{i}_d'$ and $\hat{i}_q'$from the adjustable model output. Through the adaptive law speed estimation formula (27), the estimated rotor speed$\hat{\omega}_e$is calculated. The estimated rotor speed *i*s then integrated to output the estimated rotor position angle, thereby achieving sensorless control of the motor system.

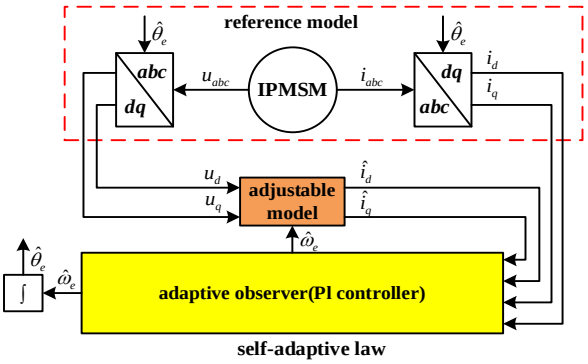

Fig. 4. Block diagram of traditional MRAS rotor position and speed estimation system

3.2. Sensorless model without electrolytic capacitor based on improved MRAS observer

Utilizing the traditional MRAS observer outlined in Section 3.1 within the ECL drive system, the d-q axis current is depicted in Fig. 5. The current observation reveals a lag in tracking the actual value, leading to significant current errors. This discrepancy can be attributed to the adaptive law, as depicted by equation (27), acting like a PI controller with limited robustness. Moreover, substantial fluctuations in various parameters within the ECL drive system at twice the power frequency introduce harmonic disturbances, impacting the accuracy of rotor position observation. Thus, it is crucial to enhance the proposed MRAS observer.

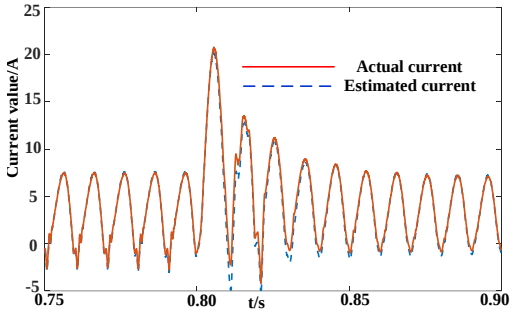

(a) traditional MRAS observer d-axis current observation value

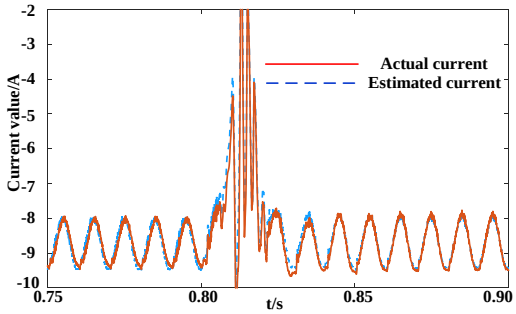

(b) traditional MRAS observer q-axis current observation value

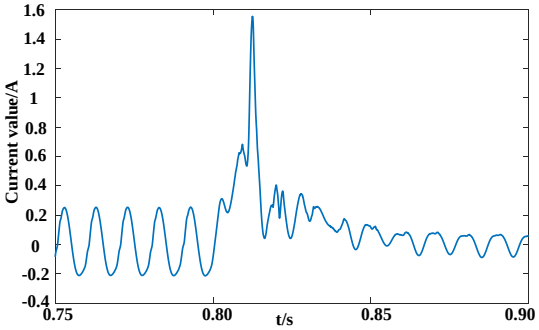

(c) traditional MRAS observer d-axis current observation error

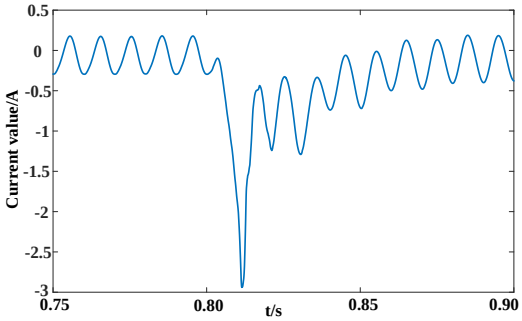

(d) traditional MRAS observer q-axis current observation error

Fig. 5. Current waveform of the traditional MRAS observer

In equation (27), the adaptive law can be viewed as a non-robust PI controller. Additionally, the variables in the electrolytic capacitor-free drive system fluctuate significantly at twice the grid-frequency, introducing harmonic interference in the signal necessary for rotor position observation, thereby affecting observation accuracy. This paper introduces super-twisting sliding-mode control to replace the PI adaptive mechanism in the observer, further enhancing the sensorless capability in a capacitor-free system.

The improved MRAS observer uses the basic form of super-twisting sliding-mode control :

$$\begin{cases} \dot{x}_1 = -k_1 |x_1|^{\frac{1}{2}} \operatorname{sgn}(x_1) + x_2 \\ \dot{x}_2 = -k_2 \operatorname{sgn}(x_1) \end{cases} \tag{29}$$

In the formula: x_1 and x_2 represent state variables, while $\dot{x}_1$ and $\dot{x}_2$ denote the derivatives of the corresponding variable; k_1 and k_2 signify the sliding-mode gains; sign ( ) denotes the symbol function.

The obtained sliding surface can be expressed as:

$$\begin{aligned} s = (\omega_e - \hat{\omega}_e)[\frac{L_d}{L_q} i_d \hat{i}_q + \frac{L_q}{L_d} i_q \hat{i}_q + \frac{\psi_f}{L_q}(i_d + \hat{i}_d) + \frac{\psi_f{}^2}{L_d L_q}] + \\ (\frac{R}{L_d} + \frac{R}{L_q})(\hat{i}_d i_q - \hat{i}_q i_d) + \frac{u_q}{L_q}(i_d - \hat{i}_d) + (\frac{R\psi_f}{L_d L_q} - \frac{u_d}{L_d})(i_q - \hat{i}_q) \end{aligned} \tag{30}$$

The speed observer is designed using super-twisting sliding-mode control. The speed estimation expression is:

$$\omega = |k||s|^{\frac{1}{2}} \operatorname{sgn}(s) + \int k \operatorname{sgn}(s) dt + \omega(0) \tag{31}$$

The convergence of the sliding surface reachability condition is verified via Lyapunov stability

analysis. By defining the state vector and constructing the Lyapunov function V, it is proven that when sliding-mode gains k1 and k2 are positive, matrices N and M become symmetric positive definite, and V is negative definite. Thus, the system achieves asymptotic stability at the equilibrium point.

When the sliding-mode gains k_1 and k_2 are both greater than zero in the super-twisting sliding-mode control equation (29), the matrices N and M are transformed into symmetric positive definite matrices, and the matrix V is negative definite. As a result, the system becomes asymptotically stable at the equilibrium point.

Considering the highly discontinuous and high-frequency characteristics of the sgn function, this leads to significant chattering in the system. Hence, replacing the sgn function with the Sigmoid function is beneficial. The Sigmoid function serves as a continuous and smooth switching function, effectively suppressing chattering. Its mathematical form is expressed as follows:

$$sig(x) = \frac{1}{1+e^{-ax}} \tag{32}$$

The Sigmoid function combines the concept of boundary layer switching from the saturation function and the concept of ideal sliding design. Linear control is employed within the boundary layer, while switching control is employed outside the boundary layer. Additionally, a compensation term is introduced to ensure continuous switching, with a larger compensation term leading to reduced vibration. The final velocity estimation can be expressed as:

$$\hat{\omega}_e = |k_1||s|^{\frac{1}{2}} sig(x) + \int_t^0 k_2 sig(x)dt + \hat{\omega}_e(0) \tag{33}$$

The current waveform of the STA-AO MRAS observer after the enhancement of the control function is depicted in Fig. 5. Comparing Fig. 5 and Fig. 6 reveals that, post enhancement of the control function, the current value converges towards the actual value, reducing the observation error to one-tenth of its original magnitude. This enhancement ultimately provides more precise position information.

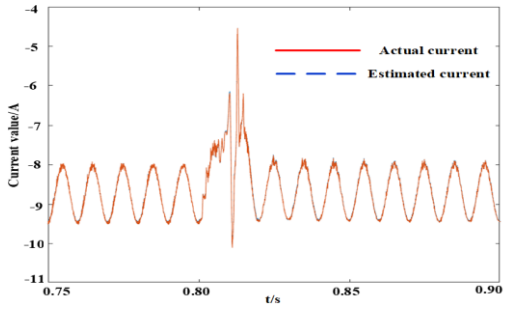

(a) STA-AO MRAS observer d-axis current observation value

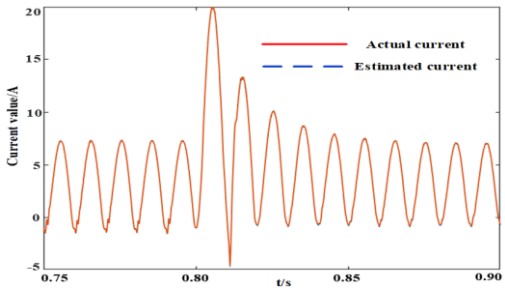

(b) STA-AO MRAS observer q-axis current observation value

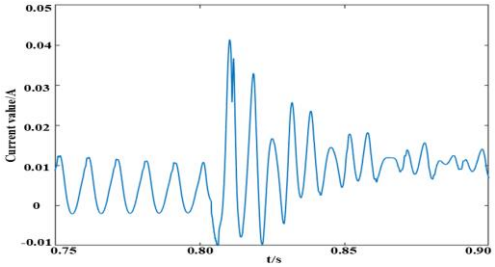

(c) STA-AO MRAS observer d-axis current observation error

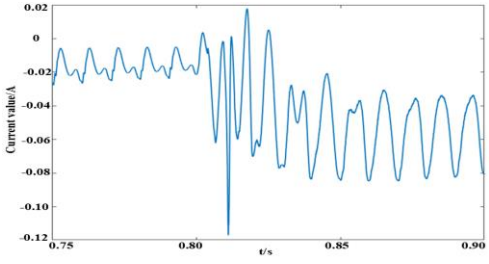

(d) STA-AO MRAS observer q-axis current observation error

Fig. 6. Current waveform of the STA-AO MRAS observer

Based on the STA-AO MRAS observer, the rotor position estimation system block diagram is shown in Fig. 7.

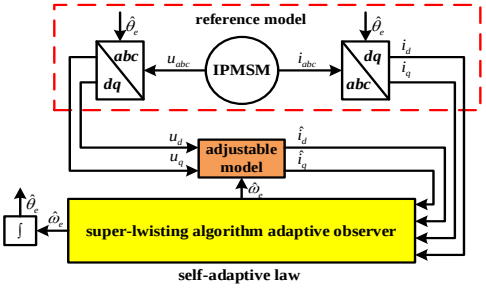

Fig. 7. Block diagram of rotor position and speed estimation system based on super-twisting sliding-mode MRAS

4. Simulation

The sensorless control scheme of the IPMSM drive with a small DC-link capacitor is shown in Fig. 8.The controller adopts STA-AO observer to suppress the DC bus voltage fluctuation caused by low capacitance and its impact on the motor performance by adjusting the relationship between bus voltage and current in real time. The power controller receives feedback signals such as bus voltage, current and load demand, calculates the deviation and generates the adjustment amount, controls the PWM signal of the inverter, and thus optimizes the current waveform and operating state of the motor. It works in conjunction with the d-axis and q-axis current controllers to improve the motor operating efficiency while ensuring torque output and excitation control, and further improves the position estimation accuracy and system robustness.

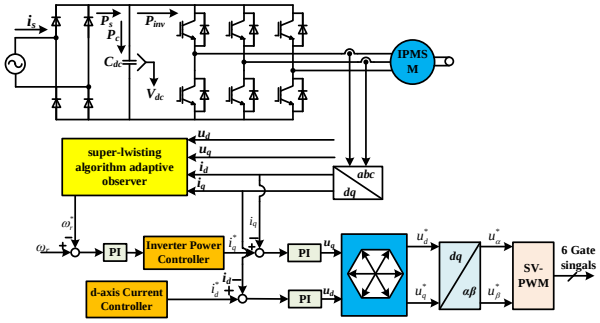

Fig. 8. IPMSM sensorless control with small DC-link capacitor.

Table 1 Experimental and simulation data

Parameter	Value
Grid frequency/Hz	50
Film capacitor/μF	20
Grid voltage/Vrms	220
Pole pairs	3
Stator resistance/Ω	0.75
dq-axis inductance/mH	7.9/11.3
Flux linkage/Wb	0.11
Rate speed/r/min	3000
Rate torque /N ṁ	3
Rate power/W	1500

To validate the efficacy of the proposed control method, a simulation model for the sensorless control strategy of a small DC-link capacitors IPMSM drive system is established based on this

method. The simulation analysis is performed in Matlab/Simulink, and experimental verification is performed using the actual platform. The system parameters for both simulation and experimentation are identical, as detailed in Table 1.

The simulation experiment compares the speed estimation strategy based on the traditional MRAS with the novel STA-AO speed estimation strategy proposed in this paper.

In this paper, the estimation accuracy of the observer is improved mainly by improving the observation accuracy of the rotor position and speed, reducing the error signal in the speed feedback loop. This reduction has an indirect effect on the improvement of the modulation waveform, thereby alleviating the impact of the high-order harmonic components of the power supply current. The harmonic components of the power supply current are directly determined by the voltage and current instructions of the motor, and the improvement of the observer accuracy is not the only decisive factor. In practical applications, low estimation accuracy will lead to the doping of harmonic signals in the position and speed feedback loops, which further affect the quality of the modulation wave through the control loop, thereby introducing harmonic components in the power supply current.

Fig. 9. (a)displays the DC-link voltage and grid-side current waveforms, respectively. The addition of the STA-AO control strategy is evident in the sine waveforms of voltage and current. Fig 8 (d) and (e) depict the Fourier analysis of motor speed and input power at 3000 rpm and 1500 W. Prior to implementing the STA-AO control strategy, higher harmonic amplitudes of DC-link voltage and grid-side current near the resonant frequency were observed. After the application of the STA-AO strategy, the total harmonic distortion (THD) of DC-link voltage and grid-side current decreased significantly from 24.45% and 37.93% to 15.54% and 29.20%, respectively, validating the effectiveness of the STA-AO control strategy in reducing harmonic amplitudes at the control frequency. This improvement comes from the reduction of position estimation error (Figure 9(d)), which reduces the 2ω_s harmonic component in the speed feedback loop. Through Lyapunov stability analysis, the STA algorithm suppresses the cumulative effect of harmonics in the control loop, thereby indirectly optimizing the spectral purity of the inverter modulation waveform.

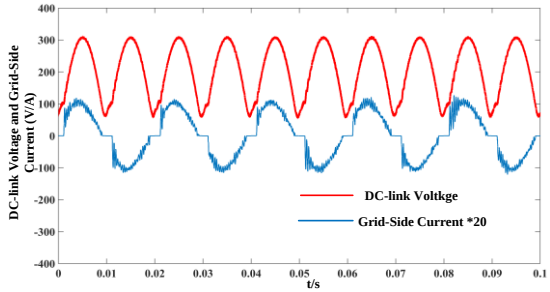

(a) DC-link voltage and Grid-Side Current Values

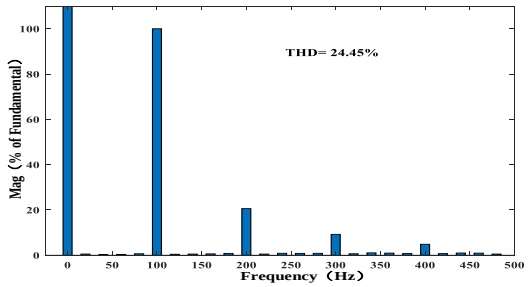

(b) FFT analysis of DC-link voltage, Traditional, THD=24.45%

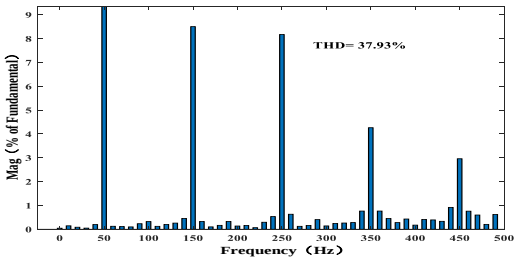

(c) FFT analysis of Grid-Side Current, Traditional, THD=37.93%

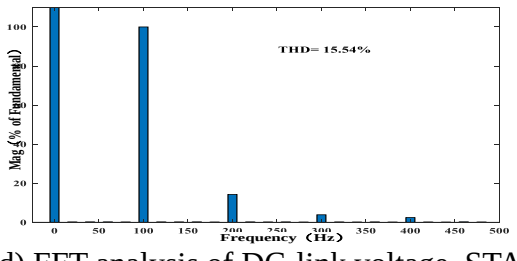

(d) FFT analysis of DC-link voltage, STA-AO,THD=15.54%

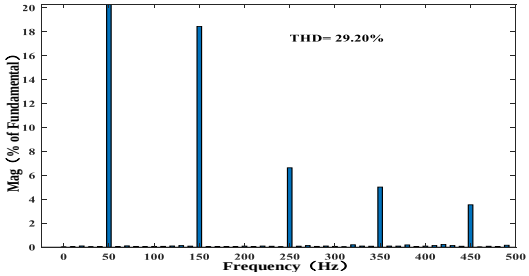

(e) FFT analysis of Grid-Side Current, STA-AO,THD=29.20%

Fig. 9. DC-link Voltage and Grid-Side Current Values of Traditional and STA-AO MRAS Observers

To compare the performance of the electrolytic capacitor-less position sensor at different speeds, the motor initially operated at 2000 rpm and then accelerated to 3000 rpm within 0.8 seconds. The simulation results illustrating motor speed, motor speed error, rotor position, and rotor position observation error under two different MRAS observers are illustrated in the figures. Throughout the process, it's evident that the enhanced MRAS observer accurately estimates the rotor position, exhibiting minimal fluctuation during motor start-up and abrupt speed changes.

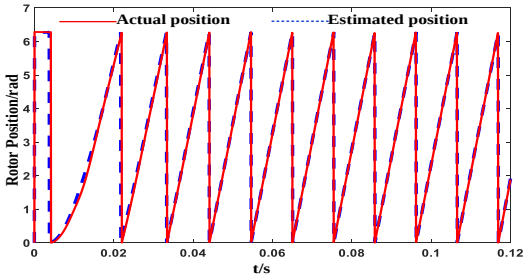

(a) traditional MRAS observer motor rotor position

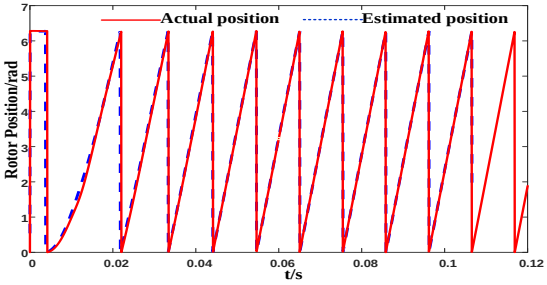

(b) STA-AO MRAS observer motor rotor position

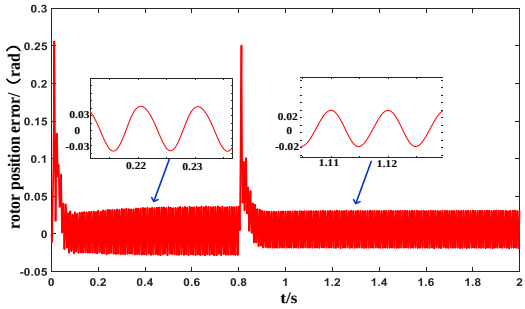

(c) traditional MRAS observer motor rotor position error

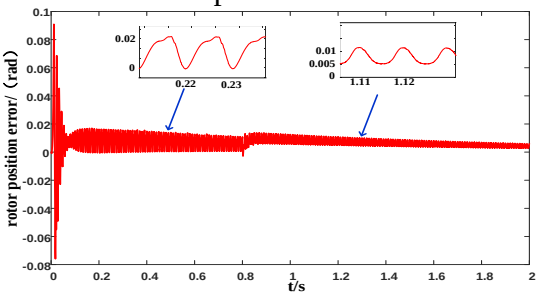

(d) STA-AO MRAS observer motor rotor position error

Fig. 10 Motor Rotor Position Waveform under two different MRAS observers

From Fig. 10.(c) and (d), it's apparent that the maximum rotor position error of the traditional MRAS observer is 0.03 radians, whereas the error for the improved MRAS observer is 0.02 radians, which tends to converge to zero. During the motor speed transition from 2000 to 3000 rpm, the rotor position error of the traditional MRAS observer sharply increases, whereas that of the improved MRAS observer remains almost unchanged and tends towards stability, approaching zero. The enhanced MRAS observer effectively estimates the rotor position of the electrolytic capacitor-less drive system with high accuracy and performance. Due to the 100 Hz fluctuation in electromagnetic torque within the electrolytic capacitor-less drive system, the speed exhibits corresponding fluctuations. From Fig. 11, during motor start-up, the traditional MRAS observer demonstrates relatively large errors between actual and estimated speeds, with a maximum error of about 60 rpm,

whereas the improved MRAS observer exhibits a maximum error of about 20 rpm. Similarly, during the transition from 2000 to 3000 rpm, the traditional MRAS observer's speed estimation sharply increases, resulting in a maximum error of 40 rpm, while the improved MRAS observer tends towards stability with a maximum error of 10 rpm, approaching convergence to zero. This further demonstrates the enhanced robustness provided by the proposed method.

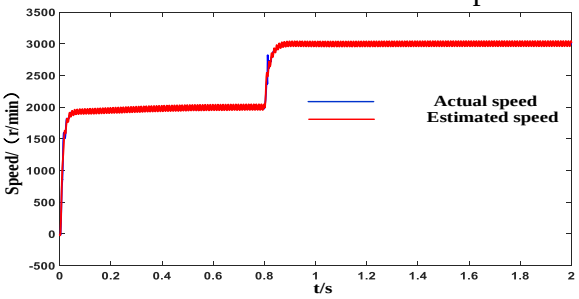

(a) traditional MRAS observer motor speed

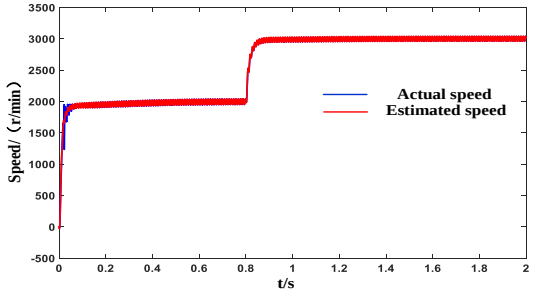

(b) STA-AO MRAS observer motor speed

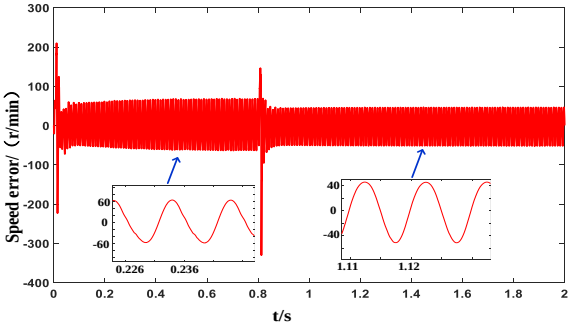

(c) traditional MRAS observer motor speed error

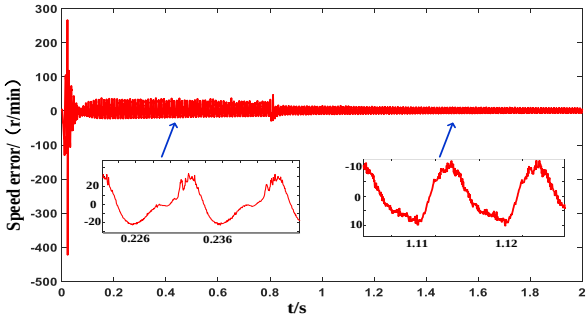

(d) STA-AO MRAS observer motor speed error

Fig. 11. Motor Rotor Speed Waveform under two different MRAS observers

5. Experiment

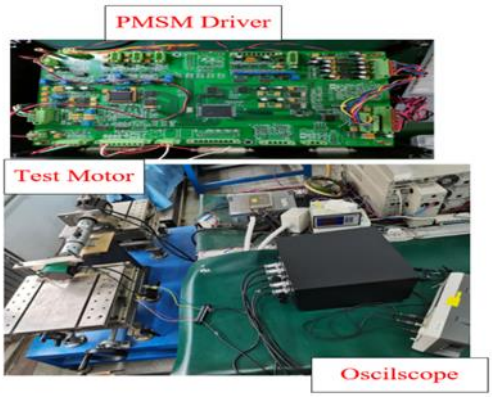

Fig. 12. Experimental platform

The experimental platform (Fig. 12) is built to validate the proposed control strategy, using the same system parameters as the simulation (Table 1). The motor is operated at 2000 rpm initially and accelerated to 3000 rpm within 0.8 seconds, with experimental data recorded via an oscilloscope. Experimental waveforms are shown in Figs. 13 and 14.

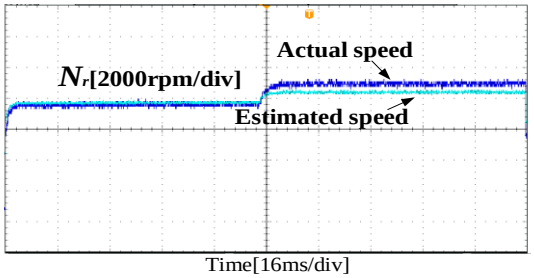

(a) traditional MRAS observer motor speed

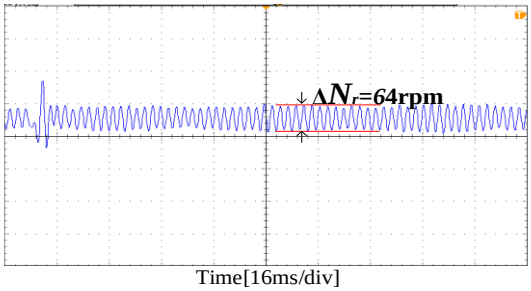

(b) traditional MRAS observer motor speed error

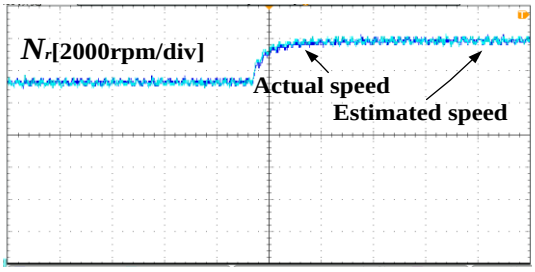

(c) STA-AO MRAS observer motor speed

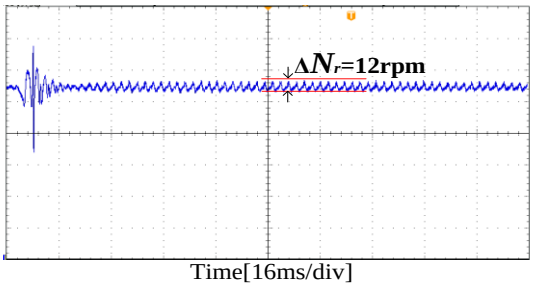

(d) STA-AO MRAS observer motor speed error

Fig. 13. Experimental Waveform of Traditional MRAS Observer Speed and STA-AO MRAS Observer Speed

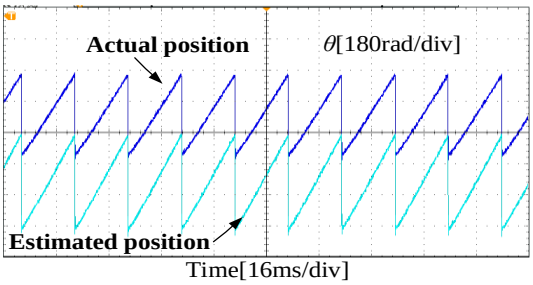

(a) traditional MRAS observer motor rotor position

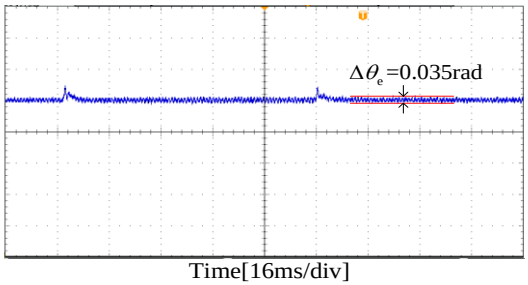

(b) traditional MRAS observer motor rotor position error

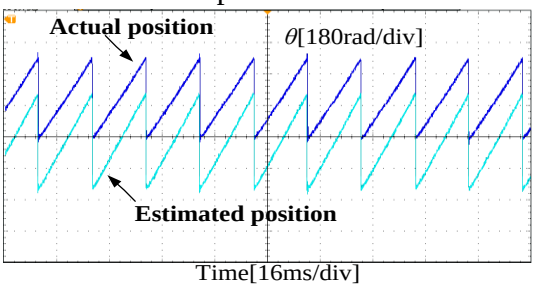

(c) STA-AO MRAS observer motor rotor position

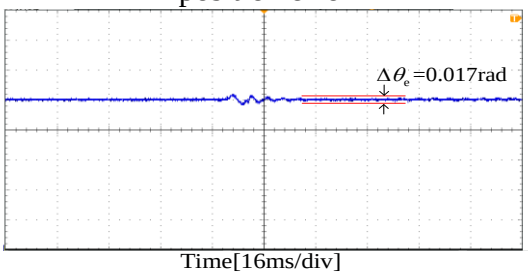

(d) STA-AO MRAS observer motor rotor position error

Fig. 14 Experimental Waveform of Traditional MRAS Observer Motor Rotor Position and STA-AO MRAS Observer Motor Rotor Position

Experimental waveforms of the speed and estimation errors for the two different MRAS observers are shown in Fig. 14. After using the STA-AO MRAS observer, the estimated speed curve basically coincides with the actual motor curve, and the speed error is significantly reduced by approximately 12r/min.

Based on the experiments and analysis above, the steady-state error and dynamic error of the

improved MRAS observer's position estimation have been reduced, effectively enhancing the control performance and stability of small DC-link electrolytic capacitor drive system.

6. Conclusions

This paper proposes an enhanced sensorless control method (STA-AO) for IPMSM drives in small DC-link capacitor systems. Experimental and simulation results confirm that the STA-AO strategy mitigates the adverse effects of variable fluctuations in electrolytic capacitor-less drives, achieving faster convergence of speed/position estimation errors to zero. It also ensures swift stability of PMSM speed under reference speed changes or load disturbances, making it well-suited for electrolytic capacitor-less drive systems.

Acknowledgments

This work has been partially Key Research and Development Program of Shaanxi Province (2023-YBGY-368123456) and Degree and Postgraduate education reform and research project of XUST (YJG 2022031).

References

[1] Kano Y, Matsui N. Sensorless control of interior permanent magnet synchronous motor: An overview and design study[C]//2017 IEEE workshop on electrical machines design, control and diagnosis (WEMDCD). IEEE, 2017: 199-207.
[2] Wei Y, Luo X, Zhu L, et al. Research on current harmonic suppression strategy of high saliency ratio permanent magnet synchronous motor based on proportional resonance controller[J]. Proceedings of the CSEE, 2021, 41(7): 2526-2538.
[3] Zhang Jian, Wen Xuhui, Li Wenshan, et al. Research on harmonic current suppression strategy of permanent magnet synchronous motor based on harmonic observer[J]. Proceedings of the CSEE,1,2020(40):10.
[4] Yamauchi K, Sanada M, Morimoto S, et al. Design IPMSM structures for enlarging high-efficiency operation area using automatic design system with new algorithm[C]//2020 23rd International Conference on Electrical Machines and Systems (ICEMS). IEEE, 2020: 23-28.
[5] Li H, Yin Q, Wang Q, et al. A novel DC-link voltage feedback active damping control method for IPMSM drives with small DC-link capacitors[J]. IEEE Transactions on Industrial Electronics, 2021, 69(3): 2426-2436.
[6] Song J, Song W, Lin H. DC-link voltage control of small capacitor PMSM drive system based on MPC algorithm[J]. International Journal of Circuit Theory and Applications, 2024, 52(1): 346-363.
[7] Zhao Nannan, Wang Gao Lin, Xu Dianguo. Review of electrolytic capacitorless drive system for permanent magnet motor[J]. Science in China, 2020, 050(007):P.863-875.
[8] Zhang Chao, XU Lei, ZHU Xiaoyong, et al. Small capacitance drive system of axial magnetic field permanent magnet motor based on virtual DC bus structure[J]. Proceedings of the CSEE, 1, 2021(41):20.
[9] Yan W, Lu W, Jiang Z, et al. Current Control of Electrolytic Capacitor-less Variable Frequency Drive System for Synchronous Reluctance Motors based on Power Balancing and Compensation[J]. IEEE Access, 2024.
[10] Khan M F, Li W, Gao Q. An effective control strategy based on DC-link voltage regulation for an electrolytic capacitor-less IPMSM drive[C]//2018 21st International Conference on Electrical Machines and Systems (ICEMS). IEEE, 2018: 1246-1251.
[11] Liu Z, Ding W, Chen S, et al. Grid-Side Current Harmonic Suppression and Power Factor Improvement Using q–Axis Damping Current Injection for PMSM Drives Without Electrolytic Capacitor[J]. IEEE Journal of Emerging and Selected Topics in Power Electronics, 2023, 11(3): 3371-3384.
[12] Hu Xin. Research on drive system and control strategy of micro-boost electrolytic capacitor permanent magnet synchronous motor[D]. Jiangsu University. ,2024.
[13] Zhang Chao, Hu Xin, Zhu Xiaoyong, et al. Research on electrolytic capacitorless drive system based on micro-boost power decoupling circuit[J]. Transactions of china Electrotechnical Society, 1, 2019(34):16.
[14] Zhang C, Gao R, Zhu X, et al. Boost-Based Active Power Decoupling Converter With Voltage Complementary for Electrolytic Capacitor-Less PMSM Drive System[J]. IEEE Transactions on Power Electronics, 2024.
[15] Ding D, Xie H, Li B, et al. Harmonic suppression based on rectified current regulation with DC-link voltage decoupling for electrolytic capacitorless PMSM drives[J]. IEEE Transactions on Power Electronics, 2023.
[16] Cai Jun, Li Pengze, Huang Yuanyuan. Second-order sliding-mode position-sensorless control based on PMSM[J].

Micromotors, 2020, 53(12):7.
[17] Duan Luyao. Research on drive system of permanent magnet motor based on electrolytic capacitor power converter[D]. Jiangsu University. ,2023.
[18] Yin, Li, Luo, et al. An Improved Sensorless Vector Control Method for IPMSM Drive with Small DC-link Capacitors[J]. Energies, 2020, 13(3):580.
[19] Arif A H, Muslim M A, Yudaingtyas E. Sensorless Field-Oriented Control (FOC) using sliding-mode Observer for BLDC Motor[J]. Kinetik: Game Technology, Information System, Computer Network, Computing, Electronics, and Control, 2024: 139-148.
[20] Zhang Zhong. Research on high power factor control technology of permanent magnet synchronous motor drive system[D].China University of Mining and Technology,2017.
[21] Lee H W, Cho D H, Lee K B. Rotor position estimation over entire speed range of interior permanent magnet synchronous motors[J]. Journal of Power Electronics, 2021, 21: 693-702.
[22] Yin Q, Li H, Luo H, et al. An improved sensorless vector control method for IPMSM drive with small DC-link capacitors[J]. Energies, 2020, 13(3): 580.
[23] Zhou He. Research on position-sensorless control system of permanent magnet synchronous motor based on MRAS[D]. Harbin University of Science and Technology. ,2022.
[24] Liao Zili, Xie Jianyi, Zhao Qijin, et al. Research on position-sensorless control method of permanent magnet synchronous motor based on improved MRAS[J]. Micromotor, 1. 2023, 21: 693-702.
[25] Zhang L, Chen Z, Yu X, et al. Sliding-mode-based robust output regulation and its application in PMSM servo systems[J]. IEEE Transactions on Industrial Electronics, 2022, 70(2): 1852-1860.
[26] Guo X, Huang S, Peng Y, et al. An improved integral sliding-mode control for PMSM drives based on new variable rate reaching law with adaptive reduced-order PI observer[J]. IEEE Transactions on Transportation Electrification, 2023, 9(3): 4503-4516.